JOURNAL OF MATERIALS SCIENCE 33 (1998) 3591–3599

Structure and ionic conduction in the $Ag_2O \cdot WO_3 \cdot TeO_2$ glass system

B. V. R. CHOWDARI, P. PRAMODA KUMARI
Department of Physics, National University of Singapore, Singapore 119260

Preparation, characterization by X-ray diffraction, differential scanning calorimetry, X-ray photoelectron spectroscopy (XPS), Raman and Fourier transform–infrared (FT–IR) spectroscopy and electrical conductivity studies have been carried out on the $y\mathrm{Ag_2O} \cdot (1-y)$ $[x\mathrm{WO_3} \cdot (1-x)\ \mathrm{TeO_2}]$ glass system. The compositional variation of the glass transition temperature and the calculated oxygen packing density values have been correlated. The conductivity at ambient temperature shows two maxima for the compositions corresponding to $y = 0.30$ and 0.40 at $x = 0.2$ and 0.4, respectively. The observed conductivity enhancement is about an order of magnitude and it is correlated to the structural modifications due to the WO_3 incorporation into the TeO_2 glass network. From the XPS spectra, the binding energies (BEs) of the Ag 3d, Te 3d, W 4f and O 1s core-levels have been determined. The O 1s spectrum is found to consist of two peaks due to the presence of $\mathrm{Te{-}_{eq}O_{ax}{-}Te}$, W–O–W, W–O, Te=O, $\mathrm{Te{-}O^{-1}}$ and $\mathrm{W{-}O^{-}1}$ oxygen species. The tungsten ions appear to exist in 5+ and 6+ oxidation states in these glasses. The proportion of the reduced tungsten ion is found to decrease with an increase in the WO_3 concentration, while that of the $\mathrm{Te{-}_{eq}O_{ax}{-}Te}$ species decreases as x increases. The FT–IR and Raman spectra of these samples reveal that the glass network consists of TeO_4, TeO_3, WO_4 and WO_6 polyhedra.

1. Introduction

Studies on oxide glasses having high ionic conductivity are interesting because of their possible use in solid state devices for energy conversion such as solid state microbatteries and fuel cells. The structural and transport properties of these vitreous materials are strongly dependent on the nature and concentration of the constituent oxides. Tellurite glasses possess physical properties which are not only interesting from the fundamental point of view, but are also important for practical applications. In theses glasses, the glass network consists of asymmetrical structural units such as TeO_4 trigonal bipyramids (tbp) and TeO_3 trigonal pyramids (tp) with a lone pair of electrons, which are quite different from other conventional glass-formers such as SiO_2, B_2O_3 and P_2O_5 [1–10]. Hence both the scientific understanding and technological applications of these glasses require a knowledge of their structures.

Braunstein *et al.* [11] reported that the dielectric properties of $0.23\mathrm{WO_3} \cdot \mathrm{TeO_2}$ glass are similar to those of WO_3 crystals. Binary tungsten–tellurite glasses have also been studied from the structural point of view, by means of X-ray and neutron diffraction and infrared and Raman spectroscopic techniques [12–17]. It was reported that the tellurium atoms were present in the deformed TeO_4 tbps. Moreover, it was assumed that the WO_4 polyhedra would substitute part of the TeO_4 tbps and that the coordination state of tungsten atoms would reduce with an increase in the WO_3 content.

In this paper, we report the thermal, electrical and structural properties of $y\mathrm{Ag_2O} \cdot (1-y)$ $[x\mathrm{WO_3} \cdot (1-x)\ \mathrm{TeO_2}]$ system, where $y = 0.30$ and 0.40 and $0 < x < 1$. This system is of interest because WO_3 is one of the transition metal oxides and is also a conditional glass former. Thus, both the glass formers in the present system are of conditional type, having different structural units, namely a TeO_4 trigonal bipyramid with a lone pair of electrons and a WO_6 octahedron.

2. Experimental procedure,

Reagent grade chemicals of TeO_2, $AgNO_3$ and WO_3 were used as starting materials. Mixtures of these materials taken in appropriate amounts were melted in a closed porcelain crucible at 973–1123 K for 15–20 min depending upon the composition. The resultant melt was then quenched by classical and fast quenching methods. Because some of the samples remained brittle, they were pulverized and pressed into pellets using a hand press by applying a pressure of 4 tons $\mathrm{cm^{-2}}$ for about 3 min. X-ray diffraction (XRD) measurements were carried out in order to determine whether any crystalline phases were present in the glasses. Differential scanning calorimetric (DSC) analysis was performed using a DSC-50 calorimeter under a nitrogen atmosphere at a heating rate of 10 °C $\mathrm{min^{-1}}$. The densities of the samples were determined by Archemedes method using isopropyl alcohol as the displacing medium.

0022–2461 © *1998 Kluwer Academic Publishers*

The electrical conductivities of the samples were measured using vacuum-evaporated gold as the blocking electrode by the complex impedance method. The conductivity measurements were carried out in the frequency range 10–10^6 Hz and over the temperature range 298–403 K using an eurotherm-controlled vacuum furnace. The electronic contribution to the conductivity was determined by the Wagner's polarization method using a Keithley 617 electrometer.

The X-ray photoelectron spectroscopic (XPS) data were recorded using a VG ESCA LAB MKII spectrometer with MgK_α X-ray source and an electron energy analyser set at a constant pass energy of 20 eV. The data were referenced to the C 1s peak (binding energy (BE) = 284.6 eV) resulting from the adventitious hydrocarbon present on the sample surface [18]. The Fourier transform infrared (FTIR) spectra were measured in the range 400–1200 cm^{-1} using a computerized spectrophotometer (Perkin–Elmer with GRAMS 2000 analyser). These spectra were obtained using spectroscopically pure KBr as the binder. The Raman spectra were obtained for the glass samples on a Renishaw Raman spectrometer with a stable 780 nm laser diode system, fibre-optic probe and the GRAMS-based software system. The Raman spectra were recorded in the range 100–1600 cm^{-1}.

3. Results

3.1. XRD and thermal analyses

The amorphous states of the prepared samples were analysed using the XRD. The observed featureless patterns showed the absence of crystalline phases only for those samples with $y = 0.30$ for $0 \leqslant x \leqslant 0.6$ and $y = 0.40$ for $0.2 \leqslant x \leqslant 0.6$, while the rest of the samples exhibited the presence of some crystalline phases even after they were prepared by the fast-quenching technique. The amorphous samples were then analysed by means of the DSC inorder to confirm their glassy character and measure the glass transition temperature, (T_g). The observed variations of the glass transition temperature with the composition are shown in Table I.

3.2. Density, Oxygen packing density and Ag^+ ion concentration

Density values of glasses in the $yAg_2O\cdot(1-y)$ $[xWO_3\cdot(1-x)\ TeO_2]$ system are shown in Table I. From the table, it is clear that the glass density, ρ, increases as the WO_3 concentration increases. The increase in the values of density is attributed to the higher molecular weight of WO_3 in comparison with that of the TeO_2, and the formation of WO_4 which occupies a smaller space than WO_6 octahedra. The values of Ag^+ ion concentration and the oxygen packing density (OPD) calculated from the density and composition are also given in Table I.

3.3. Electrical measurements

Generally, the temperature dependence of electrical conductivity of a vitreous material is due to (i) the thermal activation (the conductivity increases with temperature according to the Arrhenius Law), and (ii) the structural modification of the glass with temperature [19]. In the present case, the conductivity, σ, is studied as a function of temperature and found to obey the Arrhenius law

$$\sigma = \sigma_0 \exp\left(-\frac{E_{act}}{kT}\right) \qquad (1)$$

where σ is the conductivity, σ_0 is the pre-exponential factor, E_{act} is the activation energy, k is the Boltzmann constant and T is the temperature.

This suggests that the thermally activated mobile ion concentration is the underlying cause for the enhanced conductivity. The activation energy and pre-factor σ_0 values calculated from the Arrhenius plot are given in Table II along with the values of conductivity at 298 K. The isothermic conductivity variations with glass composition given in Fig. 1 show two maxima at $x = 0.2$ and 0.4 for both $y = 0.30$ and 0.40. The electronic conductivity values were found to be 2.7×10^{-10}, 5.6×10^{-10} and 1.24×10^{-10} $S\,cm^{-1}$ for the compositions $0.30Ag_2O\cdot0.35\,WO_3\cdot0.35\,TeO_2$, $0.30Ag_2O\cdot0.14\,WO_3\cdot0.56\,TeO_2$ and $0.40Ag_2O\cdot0.30WO_3\cdot0.30TeO_2$, respectively. These values are small compared to the observed ionic conductivity values.

TABLE I Compositions, glass transition temperatures and density values of the $yAg_2O\cdot(1-y)$ $[xWO_3\cdot(1-x)\ TeO_2]$ glass system

Ag_2O, y (mol %)	WO_3 (mol %)	TeO_2 (mol %)	x (mol %)	T_g(K)	ρ (g cm^{-3})	OPD (mol l^{-1})	Ag^+ ion concentration (mol l^{-1})
0.30	–	0.70	0.0	452.3	6.04	56.65	20.00
	0.07	0.63	0.1	485.0	6.20	58.91	19.97
	0.14	0.56	0.2	505.0	6.30	60.58	19.75
	0.21	0.49	0.3	526.7	6.42	62.43	19.61
	0.28	0.42	0.4	543.7	6.52	64.10	19.42
	0.35	0.35	0.5	561.0	6.67	66.21	19.38
	0.42	0.28	0.6	577.7	6.75	67.63	19.14
0.40	0.12	0.48	0.2	461.3	6.55	57.15	26.58
	0.18	0.42	0.3	482.0	6.63	58.58	26.33
	0.24	0.36	0.4	495.8	6.72	60.08	26.12
	0.30	0.30	0.5	508.4	6.81	61.58	25.93
	0.36	0.24	0.6	523.9	6.88	62.88	25.66

TABLE II Electrical data of the $y\mathrm{Ag_2O}\cdot(1-y)\ [x\mathrm{WO_3}\cdot(1-x)\ \mathrm{TeO_2}]$ glass system

Ag_2O, y (mol%)	WO_3 (mol%)	TeO_2 (mol%)	x (mol%)	σ at 298 K ($\mathrm{S\,cm^{-1}}$)	Log σ_0	E_{act} (eV)
0.30	–	0.70	0.0	$(8.97 \pm 0.16)\ 10^{-9}$	1.60 ± 0.12	0.576 ± 0.04
	0.07	0.63	0.1	$(5.84 \pm 0.23)\ 10^{-8}$	1.18 ± 0.04	0.491 ± 0.01
	0.14	0.56	0.2	$(8.18 \pm 0.18)\ 10^{-8}$	1.00 ± 0.03	0.475 ± 0.01
	0.21	0.49	0.3	$(3.19 \pm 0.24)\ 10^{-8}$	1.21 ± 0.03	0.516 ± 0.01
	0.28	0.42	0.4	$(8.89 \pm 0.15)\ 10^{-8}$	0.90 ± 0.05	0.466 ± 0.02
	0.35	0.35	0.5	$(4.40 \pm 0.24)\ 10^{-8}$	1.20 ± 0.02	0.510 ± 0.01
	0.42	0.28	0.6	$(6.74 \pm 0.23)\ 10^{-8}$	1.18 ± 0.03	0.492 ± 0.01
0.40	0.12	0.48	0.2	$(1.94 \pm 0.30)\ 10^{-6}$	1.50 ± 0.07	0.426 ± 0.02
	0.18	0.42	0.3	$(1.50 \pm 0.28)\ 10^{-6}$	1.42 ± 0.06	0.427 ± 0.02
	0.24	0.36	0.4	$(1.69 \pm 0.32)\ 10^{-6}$	1.60 ± 0.03	0.436 ± 0.01
	0.30	0.30	0.5	$(9.50 \pm 0.36)\ 10^{-7}$	1.72 ± 0.13	0.455 ± 0.04
	0.36	0.24	0.6	$(1.95 \pm 0.28)\ 10^{-6}$	1.42 ± 0.07	0.422 ± 0.03

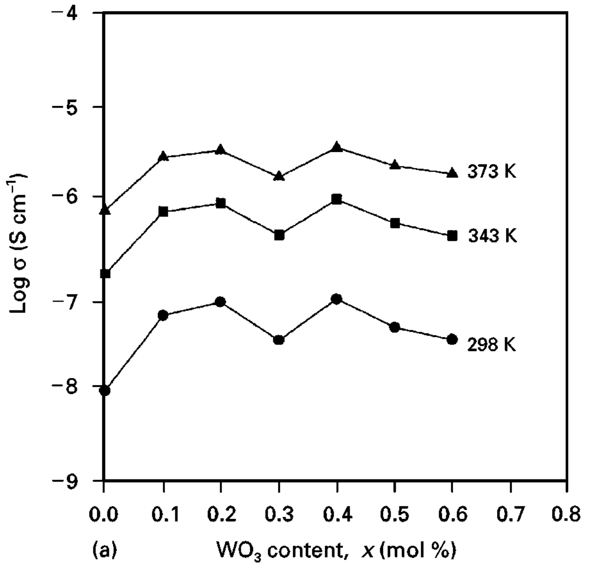

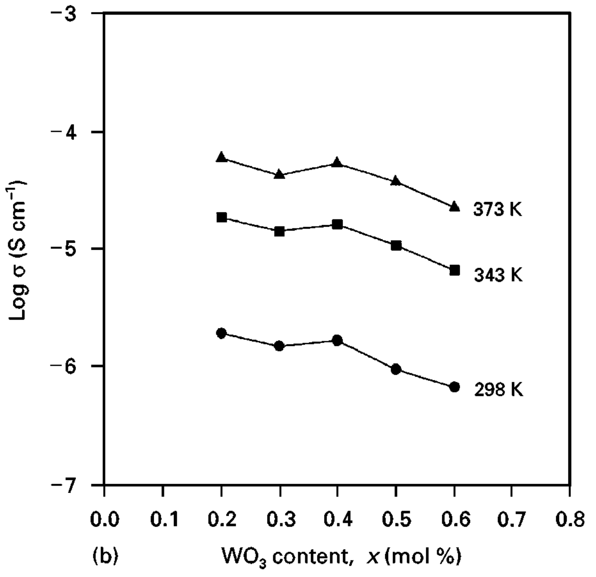

Figure 1 Compositional variation of conductivity for the $y\mathrm{Ag_2O}\cdot(1-y)[x\mathrm{WO_3}\cdot(1-x)\ \mathrm{TeO_2}]$ glass system. (a) $y = 0.30$, (b) $y = 0.40$.

3.4. X-ray photoelectron spectroscopy

The structural modifications occurring due to the partial replacement of TeO_2 by WO_3 have been studied by means of X-ray photoelectron spectroscopy. XPS is one of the modern techniques widely used for studying the surfaces of solid materials and it is well employed to identify the non-bridging oxygen atoms in oxide glasses resulting from the network modification [20, 21].

The core-level binding energies corrected for the surface charging effect, of Ag 3d, O 1s and W 4f have been determined from the respective XPS spectra, and are presented in Table III. The measured fractional peak areas of O 1s(1) denoted as $F(A_1)$ are also given in Table III. The binding energy of Ag 3d is found to remain almost constant over the entire composition range studied. The peaks due to non-bridging oxygen atoms (NBOs) and the bridging oxygen atoms (BOs) were separated by deconvoluting the O 1s spectrum into different Gaussian peaks. The O 1s(1) denotes the NBOs and O 1s(2) represents the BOs with lower and higher binding energy values, respectively [21]. Fig. 2 shows the experimental and deconvoluted O 1s XPS spectra for the $0.30\mathrm{Ag_2O}\cdot 0.28\mathrm{WO_3}\cdot 0.42\mathrm{TeO_2}$ glass.

The core-level spectrum of W 4f consists of two peaks due to electrons from spin-orbit split $4f_{7/2}$ and $4f_{5/2}$ levels. The deconvolution of each of these peaks reveals the presence of two oxidation states for the tungsten ions, namely W^{5+} and W^{6+}. The separation between the doublet $4f_{7/2}$ and $4f_{5/2}$ is found to be 2.1 eV with a peak area ratio of 1.3 whereas the separation between the core-levels of W^{5+} and W^{6+} ions is 1.0 eV. These values agree well with those reported in the literature [22]. The experimental and deconvoluted W 4f spectra of the $0.30\mathrm{Ag_2O}\cdot 0.7\mathrm{WO_3}\cdot 0.63\mathrm{TeO_2}$ glass are given in Fig. 3 as an example. Thus the doublet at the lower binding energy is attributed to the tungsten ions in the 5+ oxidation state while that at higher binding energy is attributed to those tungsten ions in the 6+ oxidation state. The proportion of tungsten ions in the 5 + oxidation state $[W^{5+}]/[W_{Total}]$, may be estimated as follows

$$\frac{[W^{5+}]}{[W_{Total}]} = \frac{\textit{Area of the } W_{4f_{7/2}} \textit{ peak attributed to } W^{5+} \textit{ ions}}{\textit{Sum of the areas of the } W_{4f_{7/2}} \textit{ peaks attributed to } W^{5+} \textit{ and } W^{6+} \textit{ions}} \qquad (2)$$

TABLE III The XPS core-level binding energies (eV) of Ag 3d, O 1s and W 4f in the $y\mathrm{Ag_2O}\cdot(1-y)\,[x\mathrm{WO_3}\cdot(1-x)\,\mathrm{TeO_2}]$ glass system with an uncertainty of ± 0.01 eV

y (mol%)	x (mol%)	Ag3d (eV)	O 1s(1) (eV)	O 1s(2) (eV)	$F(A_1)$[a]	W^{6+}		W^{5+}	
						$W4f_{7/2}$	$W4f_{5/2}$	$W4f_{7/2}$	$W4f_{5/2}$
0.30									
	0.0	367.52	529.52	530.41	0.723	–	–	–	–
	0.1	367.56	529.36	530.16	0.415	34.98	37.02	33.98	36.02
	0.2	367.82	529.87	530.93	0.783	35.07	37.19	34.07	36.09
	0.3	367.76	529.95	531.20	0.826	35.04	37.22	33.96	36.16
	0.4	367.82	529.97	531.16	0.830	35.09	37.22	34.02	36.22
	0.5	367.78	530.00	531.11	0.817	35.15	37.35	34.13	36.23
	0.6	367.87	530.03	531.14	0.816	35.18	37.38	34.12	36.32
0.40									
	0.2	367.77	529.75	530.98	0.834	34.81	36.96	33.78	35.94
	0.3	367.71	529.77	531.20	0.850	34.83	36.96	33.72	35.92
	0.4	367.80	529.82	531.17	0.838	34.85	37.03	33.82	36.00
	0.5	367.75	529.87	531.27	0.852	34.90	37.08	33.89	35.95
	0.6	367.77	529.87	531.25	0.843	34.89	37.09	33.87	36.07

[a] $F(A_1)$ denotes the fractional peak area of O 1s(1).

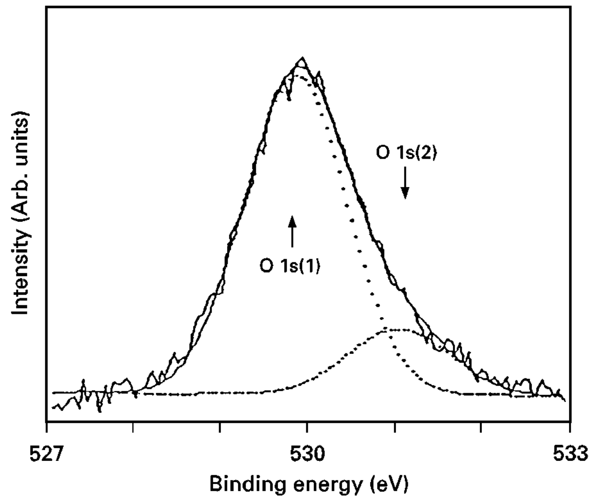

Figure 2 The experimental and deconvoluted Gaussian peaks of O 1s spectrum for the $0.30\mathrm{Ag_2O}\cdot0.28\mathrm{WO_3}\cdot0.42\mathrm{TeO_2}$ glass.

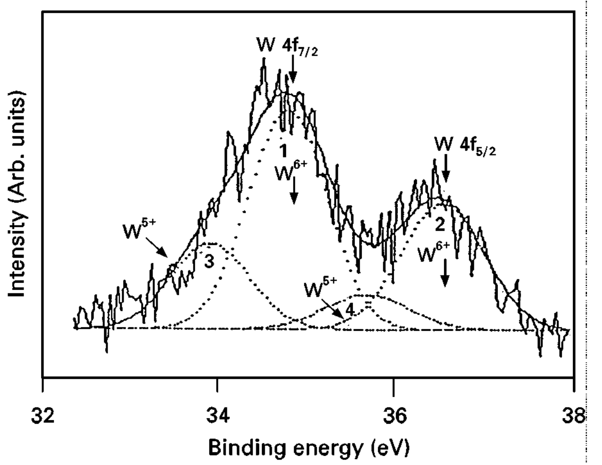

Figure 3 The experimental and deconvoluted Gaussian peaks of $W\,4f$ spectrum for the $0.30\mathrm{Ag_2O}\cdot0.07\mathrm{WO_3}\cdot0.63\mathrm{TeO_2}$ glass.

The compositional dependence of $[W^{5+}]/[W_{Total}]$ in the $y\mathrm{Ag_2O}\cdot(1-y)\;[x\mathrm{WO_3}\cdot(1-x)\;\mathrm{TeO_2}]$ glass is presented in Fig. 4 and it is evident that this ratio decreases with increase in x for both $y = 0.30$ and 0.40.

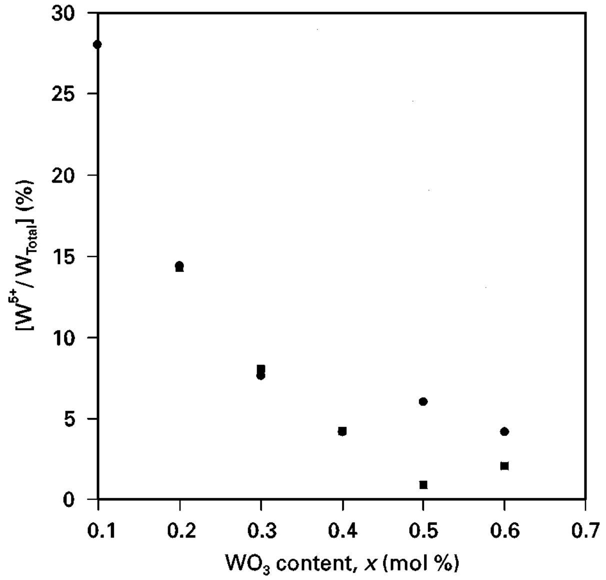

Figure 4 The proportion of tungsten ions in the 5 + oxidation state in the $y\mathrm{Ag_2O}\cdot(1-y)\;[x\mathrm{WO_3}\cdot(1-x)\;\mathrm{TeO_2}]$ glass system. for y = (●) 0.30, (■) 0.40.

The experimental and deconvoluted Te 3d XPS spectra for six different samples in the $y\mathrm{Ag_2O}\cdot(1-y)\;[x\mathrm{WO_3}\cdot(1-x)\;\mathrm{TeO_2}]$ system are shown in Fig. 5. The Te 3d spectra, deconvoluted into four Gaussian peaks, are labelled as Te 3d(1), Te 3d(2), Te 3d(3) and Te 3d(4), respectively, and are assigned to different tellurium-based structural units such as $[\mathrm{TeO_4}]$, $[\mathrm{TeO_3^-}]$, $[\mathrm{TeO_3^{2-}}]$ and [Ag–Te bond] as indicated in Table IV. These assignments have been made based on the electronegativity and the binding energy considerations [3, 4]. The binding energy values along with the measured fractional peak area of Te 3d(1) denoted as $F(A_2)$ are also given in Table IV. Because the network former $[\mathrm{TeO_2}]$ is partially replaced by another network former $[\mathrm{WO_3}]$, the fractional peak area of Te 3d(1) denoted as $F(A_2)$ is found to remain almost constant up to $x = 0.3$, and beyond that the peak intensities of Te 3d(2), Te 3d(3), Te 3d(4) increase with the corresponding decrease in the intensity of

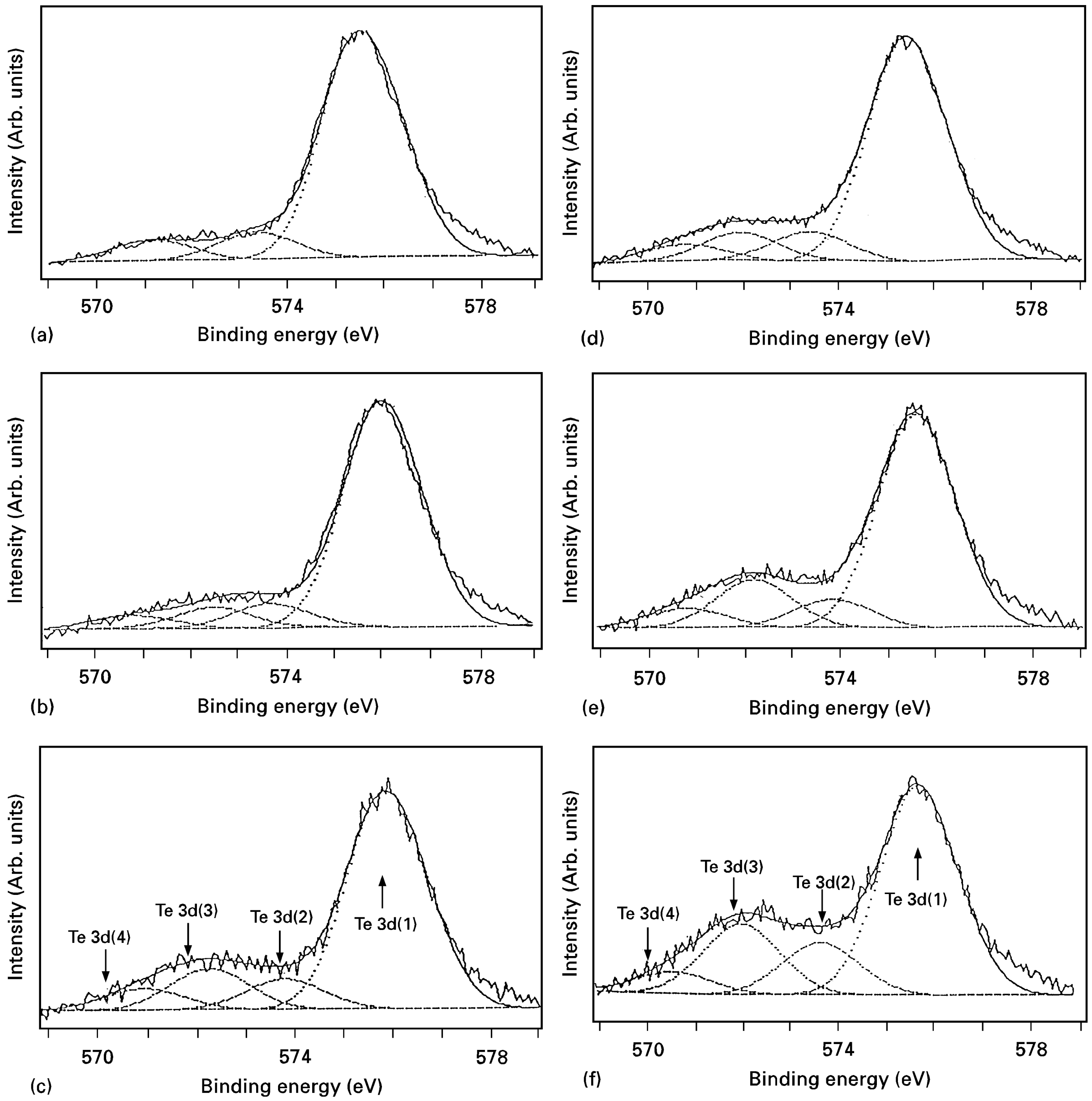

Figure 5 The experimental and deconvoluted Gaussian peaks of Te 3d spectra for few glasses in the $y\mathrm{Ag_2O}\cdot(1-y)\,[x\mathrm{WO_3}\cdot(1-x)\,\mathrm{TeO_2}]$ system. (a–c) $y = 0.30$, (d–f) $y = 0.40$. (a, d) $x = 0.2$, (b, e) $x = 0.4$, (c, f) $x = 0.6$.

TABLE IV The XPS core-level binding energies (eV) of Te 3d in the $y\mathrm{Ag_2O}\cdot(1-y)\,[x\mathrm{WO_3}\cdot(1-x)\,\mathrm{TeO_2}]$ glass system with an uncertainty of ± 0.01 eV

y (mol %)	x (mol %)	Te 3d(1) [$\mathrm{TeO_4}$] (eV)	Te 3d(2) [$\mathrm{TeO_3^-}$] (eV)	Te 3d(3) [$\mathrm{TeO_3^{2-}}$] (eV)	Te 3d(4) [Ag–Te bond] (eV)	$F(\mathrm{A_2})$[a]
0.30						
	0.0	575.42	573.22	–	571.92	0.863
	0.1	575.56	573.96	–	571.96	0.857
	0.2	575.77	573.87	–	572.07	0.826
	0.3	575.76	573.97	–	572.16	0.812
	0.4	575.82	573.82	572.82	571.42	0.795
	0.5	575.83	573.83	572.83	571.43	0.741
	0.6	575.83	574.04	572.73	571.60	0.701
0.40						
	0.2	575.47	573.72	572.52	571.52	0.753
	0.3	575.46	574.00	572.68	571.38	0.710
	0.4	575.50	574.00	572.60	571.40	0.694
	0.5	575.55	573.95	572.55	571.35	0.637
	0.6	575.52	573.77	572.37	571.17	0.594

[a] $F(\mathrm{A_2})$ denotes the fractional peak area of Te 3d(1).

Te 3d(1) peak as the WO_3 content increases. A similar trend has also been observed in the silver molybdotellurite glasses [23]. It is clear from Table IV that there is a considerable decrease in the $F(A_2)$ values beyond $x = 0.3$. On the other hand, for $y = 0.40$, it can be seen from Table IV that the fractional peak area of Te 3d(1) i.e. $F(A_2)$ remains constant for $x \leqslant 0.3$. As more and more TeO_2 structural units are replaced by WO_3 there is a decrease in the $F(A_2)$ value. However, these observations indicate that WO_3 acts as a modifier to the TeO_2 units and contributes for the formation of NBOs.

3.5. Fourier transform–infrared spectroscopy and Raman spectroscopy

The Fourier transform–infrared transmittance spectra for various glass samples in the $0.30Ag_2O \cdot 0.70 [xWO_3 \cdot (1-x)\ TeO_2]$ system are shown in Fig. 6. The observed absorption bands at 780 and 660 cm^{-1} in the case of crystalline TeO_2 have been assigned to the stretching vibrations of $Te\text{–}_{eq}O$ and $Te\text{–}_{ax}O$ bonds in the TeO_4 units, respectively [15, 23]. With the partial replacement of TeO_2 by WO_3 a new band at around 930 cm^{-1} appears and this may be assigned to the symmetric vibrations of WO_4 tetrahedra. The relative intensity of this band increases with respect to the band at 660 cm^{-1}.

It has been reported that the Raman spectrum of pure TeO_2 glass consists of five Gaussian peaks at 773, 716, 660, 600 and 450 cm^{-1}, respectively [13, 17]. The Raman studies on binary alkali tellurite glasses have shown that the observed peaks in the 720–780 cm^{-1} range may be assigned to TeO_3 tp with NBOs. Similarly, those peaks observed in the 610–680 cm^{-1} range and at 460 cm^{-1} may be ascribed to the stretching mode of TeO_4 tbp with BO and the bending mode of Te–O–Te or O–Te–O linkages, respectively. In the case of binary tungsten tellurite glasses, new peaks were observed at 930, 850 and 350 cm^{-1} in addition to those peaks at 770, 670 and 460 cm^{-1} due to the TeO_3 tp and TeO_4 tbp units [13, 14, 17]. The relative intensity of the 770 cm^{-1} peak against the 670 cm^{-1} peak apparently increased, whereas that of the 460 cm^{-1} peak decreased with an increase in the WO_3 content (similar to the alkali tellurite glasses) suggesting the conversion of TeO_4 tbp into TeO_3 tp in the WO_3–TeO_2 system. The observed sharp peak at 930 cm^{-1}, broad peaks at 850 and 350 cm^{-1} represent the characteristic bands of tungstate glasses which may be attributed to $W\text{–}O^-$, $W{=}O$ in the WO_4 tetrahedra, W–O–W in WO_4 or WO_6 units and corner shared WO_6 octahedra, respectively.

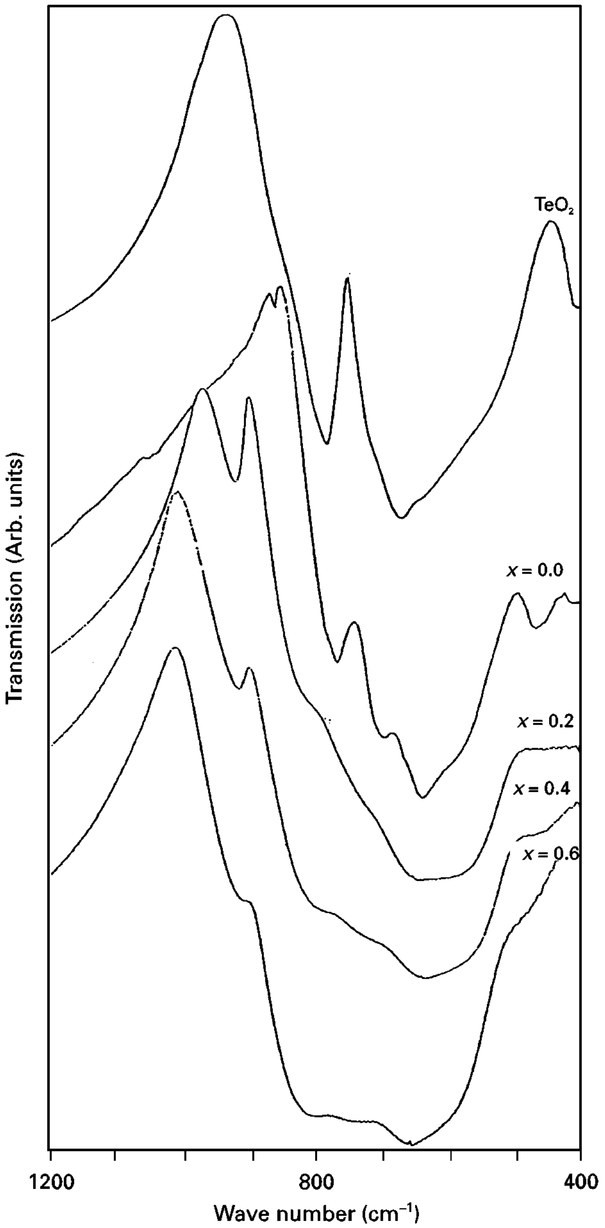

Figure 6 The infrared transmittance spectra for various glasses in the $0.30Ag_2O \cdot 0.70[xWO_3 \cdot (1-x)\ TeO_2]$ system, for $y = 0.30$.

The observed Raman spectra of the $0.30Ag_2O \cdot 0.70 [xWO_3 \cdot (1-x)\ TeO_2]$ glasses are shown in Fig. 7. It can be seen that, the addition of WO_3 results in a new strong peak around 900 cm^{-1} and a weak peak at 350 cm^{-1}, whereas the intensity of the peak observed at 460 cm^{-1} is found to decrease as the WO_3 content increases. For the qualitative analysis of the intensity ratio, the Raman spectra observed in the range 200–1000 cm^{-1} have been deconvoluted into the component bands. The experimental and the deconvoluted Raman spectra for the $0.30Ag_2O \cdot 0.14WO_3 \cdot 0.56TeO_2$ glass are shown in Fig. 8. In the present ternary system, $Ag_2O \cdot WO_3 \cdot TeO_2$, the Raman spectra consists of eight Gaussian peaks A, B, C, D, E, X, Y and Z, as listed in Table V. The peak positions of Y, X and Z are shifted to lower wave numbers in the ternary system and their relative intensities increase with the WO_3 content. The intensity ratios I_{720}/I_{660} and I_{780}/I_{660} of the Raman peaks may represent the ratio of the fractions of TeO_3 tp and TeO_4 tbp: TeO_3/TeO_4. Hence, the compositional variation of the intensity ratios I_{720}/I_{660} and I_{780}/I_{660} are shown in Fig. 9. It is seen that in the binary systems WO_3–TeO_2 and Ag_2O–TeO_2, both I_{720}/I_{660} and I_{780}/I_{660} increases with WO_3 and Ag_2O content. This variation suggests that there is a continuous transformation of the TeO_4 tbp into TeO_3 tp units. In the case of WO_3–TeO_2 system the variation may also result from the formation of the Te–O–W linkage. However, in the

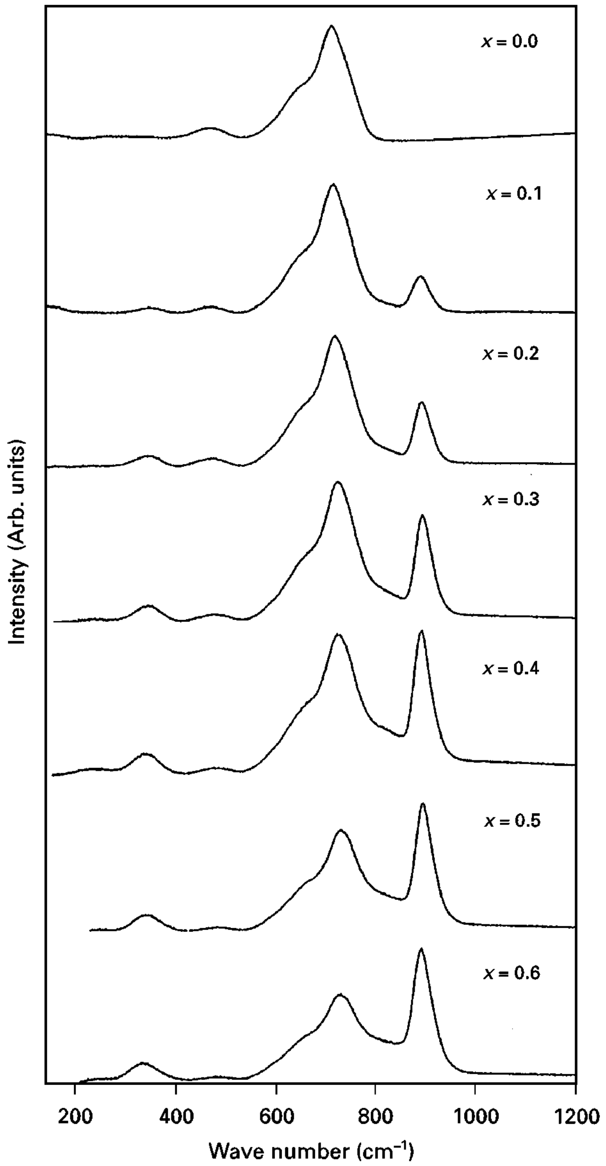

Figure 7 The Raman spectra of the $0.30Ag_2O \cdot 0.70[xWO_3 \cdot (1 - x) TeO_2$ glasses.

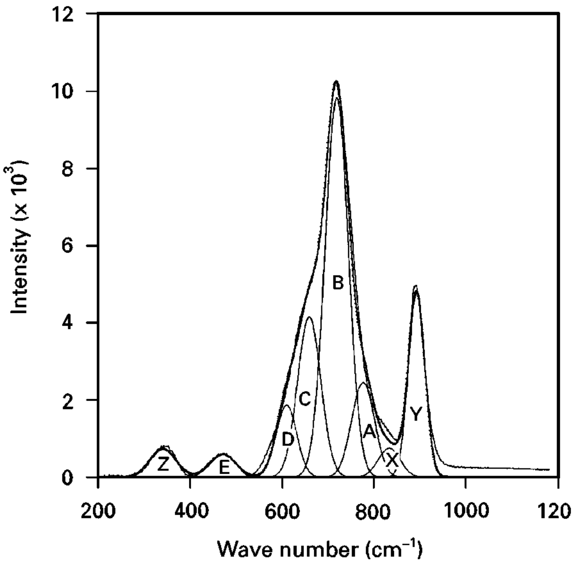

Figure 8 The experimental and deconvoluted Raman spectra of the $0.30Ag_2O \cdot 0.14WO_3 \cdot 0.56TeO_2$ glass.

TABLE V Raman band assignments for the $Ag_2O \cdot WO_3 \cdot TeO_2$ glasses

Peak	Wave number (cm^{-1})	Vibrational mode
A	770–780	Stretching vibrations of TeO_3 tp
B	720–760	Stretching vibrations of TeO_3 tp
C	650–665	Stretching vibrations of TeO_4 tbp
D	600–612	Stretching vibrations of TeO_4 tbp
E	460–500	Bending vibrations of Te–O–Te or O–Te–O linkages
X	830–835	Stretching vibrations of W–O–W in the WO_4 or WO_6 units
Y	890–900	Stretching vibrations of $W–O^-$ and $W = O$ in the WO_4 tetrahedra
Z	340–350	Bending vibrations of W–O–W in the WO_6 units

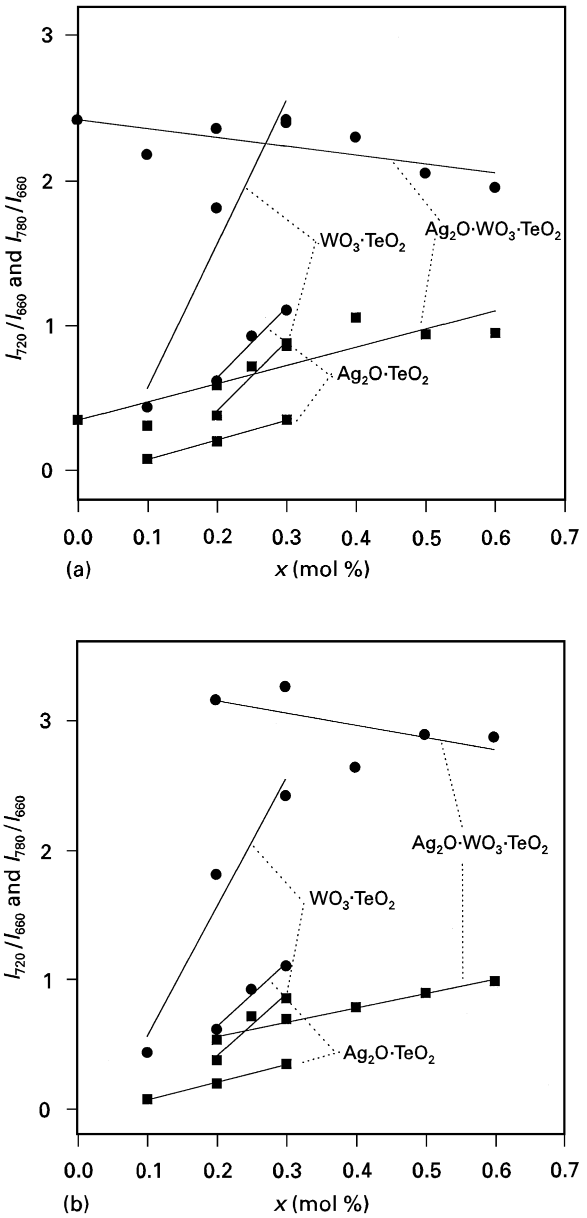

Figure 9 The intensity ratios of the deconvoluted Raman peaks for the $Ag_2O \cdot TeO_2$, $WO_3 \cdot TeO_2$ and $yAg_2O \cdot (1 - y)$ $[xWO_3 \cdot (1 - x) TeO_2]$ glasses. (a) $y = 0.30$, (b) $y = 0.40$. (●) I_{720}/I_{660}, and (■) I_{780}/I_{660}.

$Ag_2O \cdot WO_3 \cdot TeO_2$ ternary system, it is noticed that I_{780}/I_{660} increases, whereas I_{720}/I_{660} decreases with the WO_3 content for both $y = 0.30$ and 0.40. This variations can be visualized as follows: in a system like $Ag_2O \cdot WO_3 \cdot TeO_2$, the network modification by Ag_2O could result in the transformation of TeO_4 and TeO_3 along with the creation of NBOs. On the other hand, the modification of the Te–O–W linkage by Ag_2O would cause a decrease in I_{720}/I_{660}.

4. Discussion

4.1. The glass transition temperature

Table I shows that the variation in T_g is linear with respect to the WO_3 content, indicating that there is a formation of Te–O–W linkages due to the addition of WO_3 into TeO_2. Moreover, the fact that the calculated OPD also varies linearly, implies that the coordination state of W^{6+} is independent of the glass composition. It is seen that glasses with $y = 0.30$ have higher T_g values compared to those with $y = 0.40$. This may be attributed to the existence of a high degree of polymerization in the former. On the other hand, as the amount of network modifier increases (i.e. as y increases), more and more network bonds would break, leading to the formation of non-bridging oxygen atoms and decrease of T_g values. However, the partial replacement of a higher cross-link density (the value being 3) and higher bond energy for a substance having a lower cross-link density and a lower bond energy, may lead to an increase in T_g, as observed in the present investigation.

4.2. The glass structure

Based on a structural study [2] of tellurite glasses, one can conclude that (i) the basic building unit of TeO_2 glass is a trigonal bipyramid (tbp) TeO_4, and (ii) upon addition of modifier oxides, the tbp would gradually change through TeO_{3+1} to trigonal pyramid TeO_3. Therefore, the continuous structural transition is quite unique to tellurite glasses and is not known to occur in other oxide glasses like, phosphate, borate, silicate, etc.

The $Ag_2O \cdot WO_3 \cdot TeO_2$ glasses may consist of TeO_4 polyhedra and WO_6 octahedra sharing corners, according to the Zachariasen rules. The WO_6 and TeO_4 polyhedra may therefore be connected by $Te–_{eq}O_{ax}–W$ linkages. The $Te–_{eq}O_{ax}–W$ linkages are expected to form from the $Te–_{eq}O_{ax}–Te$ and W–O–W species, because both tellurium and tungsten ions have comparable electronegativity values (2.1 and 2, respectively) and can therefore substitute for each other in bonding with oxygen atoms. Moreover, the observed increase in the relative intensity of the Raman peak A with respect to the peak C suggests that there is a formation of Te–O–W linkages. These linkages may be modified by Ag_2O according to the following reactions

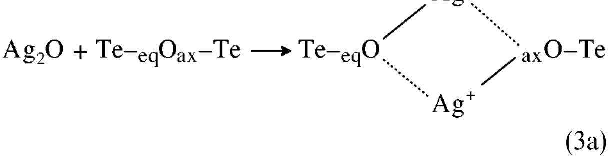

$$Ag_2O + Te–_{eq}O_{ax}–Te \longrightarrow Te–_{eq}O \begin{smallmatrix} Ag^+ \\ \\ Ag^+ \end{smallmatrix} {}_{ax}O–Te \qquad (3a)$$

or

$$Ag_2O + T–_{eq}O_{ax} – Te \rightarrow 2Te–_{eq}O^-Ag^+ \text{ or } 2Te–_{ax}O^-Ag^+ \qquad (3b)$$

and

$$Ag_2O + Te–_{eq}O_{ax} – W \rightarrow Te–_{eq}O\ ^-Ag^+ \text{ or } Te–_{ax}O^-Ag^+ + W–O^-Ag^+ \qquad (4)$$

As a result, tellurium tetrahedra with one, two or three NBOs may be formed. Hence, the oxygen species such as $Te–_{eq}O_{ax}–Te$, Te = O, Te–O–W, W = O, $W–O^-Ag^+$, $Te–_{eq}O^-Ag^+$ and $Te–_{ax}O^-Ag^+$ may be present in $Ag_2O \cdot WO_3 \cdot TeO_2$ glasses. Evidence of these structural modifications can be observed as the variation in the intensities of Raman peaks A and B with respect to that of C and D and E.

4.3. Ionic conductivity

In the case of ionic glasses, the structure is known to influence the potential barriers for the transport of mobile ions and the mobile ion concentration. Therefore, the structural information derived for the tellurite glasses, is important from the point of view of ionic conductivity, because the $TeO_4 \rightarrow TeO_3$ transformation involves the continuous creation of non-bridging oxygens which are responsible for the conduction.

Generally, in silver oxide-based glasses, the main conductivity mechanism is due to thermally activated hopping of Ag^+ ions [24]. In the present case, as x (the WO_3 content) increases, the activation energy decreases, probably due to the decrease in the barrier heights of the potential wells as a consequence of the coulombic interactions between the mobile charges. However, the pre-factor σ_0 remains almost constant, because it is proportional to the free-carrier concentration. Therefore, we can conclude that the variations observed in the conductivity are mainly due to the changes in the activation energy.

From Fig. 1, it is clear that the conductivities of samples with $y = 0.40$ are large compared to that with $y = 0.30$. The available free carriers (i.e. Ag^+ ions) which are responsible for the conductivity are more in samples with $y = 0.40$ than those in samples with $y = 0.30$, as given in Table II. The observed two maxima in conductivity correspond to the two minima in the activation energy as given in Table II. Moreover, it is well known that the conductivity of an ion-conducting glass would generally increase with increasing concentration of non-bridging oxygen atoms, because the formation of NBOs would make the glass structure more open and reduce the jump distance of the mobile ions. From the XPS analysis it is clear that the concentration of non-bridging oxygen atoms shows two maxima corresponding to those two compositions for which the conductivity maxima have been observed. In addition, as y increases, the dimensionality of the network is found to distintegrate to a lower value, favouring the conductivity enhancement. However, these observations seem to justify that the conductivity variations may be caused by thermal activation and structural changes occurring within the glass network.

5. Conclusion

The $y\mathrm{Ag_2O}\cdot(1-y)[x\mathrm{WO_3}\cdot(1-x)\ \mathrm{TeO_2}]$ glass system was characterized through XRD, DSC, XPS, Raman, FT–IR and complex impedance spectroscopic studies. The changes observed in the glass transition temperature with the WO_3 content were correlated to the calculated oxygen packing density. The conductivity at 298 K showed two maxima for both $y = 0.30$ and 0.40 at $x = 0.2$ and 0.4. The conductivity enhancement was correlated to the structural modifications occurring due to the WO_3 incorporation into the glass network. The bridging and non-bridging oxygen atoms were distinguished from the deconvoluted O 1s XPS spectra. The deconvolution of the W 4f spectrum showed that the proportion of W^{5+} would decrease with an increase in the WO_3 concentration. The deconvoluted Gaussian peaks of the Te 3d XPS spectra were assigned to the various tellurium based structural units. The Raman and FT–IR spectra of these samples showed that the glass network was made up of TeO_4, TeO_3, WO_4 and WO_6 polyhedra.

Acknowledgements

The authors thank Professor K. L. Tan for his interest in this work and Mr H. K. Wong for his help in taking XPS spectra. Thanks are also due to Dr Shen and Mr Wong for their help in taking Raman spectra.

References

1. P. BALAYA and C. S. SUNANDANA, in "Recent advances in Fast ion conducting materials and devices", edited by. B. V. R. Chowdari, Q. Liu and L. Chen (World Scientific, Singapore, 1990) p. 539.
2. T. SEKIYA, N. MOCHIDA, A. OHTSUKA and M. TONOKAWA, *J. Non-Cryst. Solids* **144** (1992) 128.
3. B. V. R. CHOWDARI and P. PRAMODA KUMARI, *ibid.* **197** (1996) 31.
4. *Idem*, *Solid State Ionics* **86–88** (1996) 521.
5. G. D. L. K. JAYASINGHE, D. COPPO, P. W. S. K. BANDARANAYAKE and J. L. SOUQUET, *ibid.* **76** (1995) 297.
6. P. BALAYA and C. S. SUNANDANA, *J. Non-Cryst. Solids* **175** (1994) 51.
7. T. YOKO, K. KAMIYA, H. YAMADA and K. TANAKA, *J. Am. Ceram. Soc.* **71** (1988) C70.
8. T. NISHIDA and Y. TAKASHIMA, *Nucl. Instrum. Meth. Phys. Res.* **B76** (1993) 397.
9. R. E. MALLAWANY, *J. Mater. Sci. Mater. Electron.* **6** (1995) 1.
10. S. NEOV, V. KOZHUKHAROV, I. GERASIMOVA, K. KREZHOV and B. SIDZHIMOV, *J. Phys. C* **12** (1979) 2475.
11. R. BRAUNSTEIN, I. LEFKOWITZ and J. SNARE, *Solid State Commun.* **28** (1978) 843.
12. V. KOZHUKHAROV, S. NEOV, I. GERASIMOVA and P. MIKULA, *J. Mater. Sci.* **21** (1986) 1707.
13. T. SEKIYA, N. MOCHIDA and S. OGAWA, *J. Non-Cryst. Solids* **176** (1994) 105.
14. M. TATSUMISAGO, T. MINAMI, Y. KOWADA and H. ADACHI, *Phys. Chem. Glasses* **35** (1994) 89.
15. Y. DIMITRIEV, V. DIMITROV and M. ARANUDOV, *J. Mater. Sci.* **18** (1983) 1353.
16. I. SHALTOUT, Y. TANG, R. BRAUNSTEIN and A. M. ABU-ELAZM, *J. Phys. Chem. Solids* **56** (1995) 141.
17. Y. HEMEI, A. OSAKA, T. NANBA and Y. MIURA, *J. Non-Cryst. Solids* **177** (1994) 164.
18. D. BRIGGS and M. P. SEAH, Eds. in "Practical Surface Analysis by Auger and X-ray Photoelectron Spectroscopy" (Wiley, New York, 1983).
19. C. JULIEN and M. MASSOT, in "Microionics-solid state integrable Batteries", edited by M. Balkanski (Elsevier Science, Amsterdam, 1991) p. 173.
20. D. S. GOLDMAN, *J. Phys. Chem. Solids* **27** (1986) 128.
21. R. GRESCH, W. MULLER-WARMUTH and H. DUTZ, *J. Non-Cryst. Solids* **34** (1979) 127.
22. T. H. FLEISCH and G. J. MAINS, *J. Chem. Phys.* **76** (1982) 780.
23. B. V. R. CHOWDARI and P. PRAMODA KUMARI, *J. Phys. Chem. Solids* **58** (1997) 515.
24. S. W. MARTIN, *J. Am. Ceram. Soc.* **74** (1991) 1767.

Received 23 June 1997
and accepted 22 April 1998